

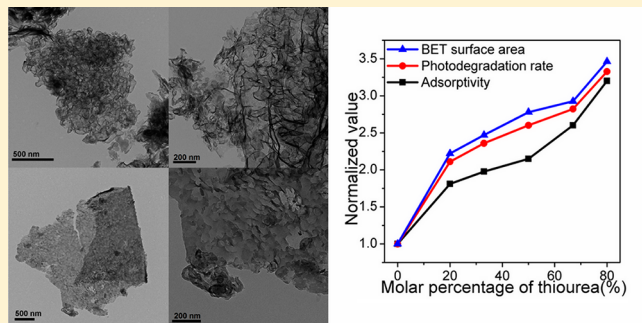
Nanoporous Graphitic Carbon Nitride with Enhanced Photocatalytic Performance

Jing Xu,[†] Yajun Wang,[†] and Yongfa Zhu*

Department of Chemistry, Beijing Key Laboratory for Analytical Methods and Instrumentation, Tsinghua University, Beijing, 100084, China

Supporting Information

ABSTRACT: Nanoporous g-C₃N₄ (npg-C₃N₄) with high surface area was prepared by a bubble-templating method. A higher calcination heating rate and proportion of thiourea can result in a larger surface area and better adsorption and photodegradation activities of npg-C₃N₄. Compared with the bulk g-C₃N₄, the adsorption capacity for the target pollutants and photocatalytic degradation and photocurrent performances under visible light irradiation of npg-C₃N₄ were greatly improved. The optimal photodegradation activity of npg-C₃N₄ was 3.4 times as high as that of the bulk g-C₃N₄. The enhanced activities of npg-C₃N₄ can be attributed to the larger number of surface active sites, improved separation of photogenerated electron–hole pairs, and higher efficiency of charge immigration.



INTRODUCTION

Graphite-like carbon nitride (g-C₃N₄) has drawn plenty of scientific interest due to its potential application in solar energy conversion, photosynthesis, electrocatalysis, and bioimaging application.^{1–5} g-C₃N₄ has the ability of water splitting and organic pollutants degradation under visible light irradiation.^{1,2} However, the photocatalytic activity of the bulk g-C₃N₄ is limited by its low surface area and quantum efficiency.⁶ Many potential applications of g-C₃N₄ are emerging as research is carry on in structure engineering and activity improving.^{7–21}

Recently, porous g-C₃N₄ has been successfully prepared via templating methods, such as soft-templating (self-assembly) and hard-templating (nanocasting) methods.^{22–32} Compared with the bulk g-C₃N₄, porous g-C₃N₄ possesses controllable morphology, tunable pore diameter, higher surface area, and a larger number of active sites on the surface, which can show potential in an even wider range of applications.^{33–36} Wang et al. reported the synthesis of mesoporous g-C₃N₄ (mpg-C₃N₄) with a three-dimensionally (3D) interconnected framework using SiO₂ as the template, which shows a remarkable improvement in H₂ evolution activity over the bulk g-C₃N₄.³⁵ Chen et al. applied SBA-15 as the hard template to yield ordered mpg-C₃N₄ with a large surface area and uniform pore size, which also exhibits improved activity for photochemical reduction of water.²⁶

However, the soft-templating method may retain some amount of carbon residue from the templating polymers in porous g-C₃N₄ which can affect its catalytic activity.⁶ Besides, the process of the hard-templating method is inconvenient and not environmentally friendly as the silica template needs to be

removed with aqueous ammonium bifluoride (NH₄HF₂) or hydrogen fluoride (HF).⁶

Herein, our group applied an easy and nontoxic bubble-templating method to synthesize nanoporous g-C₃N₄ (npg-C₃N₄) using dicyandiamide as the precursor and thiourea as the bubble template. Thiourea can decompose into gas bubbles during calcination with no need for extra removal, which results in formation of npg-C₃N₄. The structural properties of npg-C₃N₄ were systematically characterized. The adsorption capacity for the target pollutants and photocatalytic degradation and photocurrent performances under visible light irradiation were also investigated.

MATERIALS AND METHODS

Synthesis of Nanoporous g-C₃N₄ Photocatalysts. Dicyandiamide and thiourea (Tianjin Fuchen Chemical Reagents Factory, China) were ground in a ball mill for 50 min at 300 r/min, respectively. A 2.5 g amount of the milled dicyandiamide and thiourea mixture in an appropriate molar ratio was mixed carefully with a mortar and then placed in a 50 mL crucible. The npg-C₃N₄ was synthesized by heating the above mixture in a muffle furnace in air under certain calcination parameter settings as follows: from room temperature (RT) to 300 °C, the heating rate was 8 °C·min⁻¹; from 300 to 500 °C, the heating rate was 2 °C·min⁻¹; from 500 to 550 °C, the heating rate was 1 °C·min⁻¹; it was finally heated at 550 °C for 4 h. According to this process, npg-C₃N₄ prepared in different thiourea molar percentages of 20%, 33%, 50%, 67%, and 80% were named as 20%, 33%, 50%, 67%, and 80%, respectively. The bulk g-C₃N₄ was also

Received: June 16, 2013

Revised: July 26, 2013

Published: July 27, 2013

prepared by heating dicyandiamide in a muffle furnace under the same calcination parameter settings in air.

Characterization. Samples were characterized by powder X-ray diffraction (XRD) on a Bruker D8-advance X-ray diffractometer at 40 kV and 40 mA for monochromatized Cu K α ($\lambda = 1.5406 \text{ \AA}$) radiation. The Brunauer–Emmett–Teller (BET) specific surface area and pore size distribution of the samples were characterized by nitrogen adsorption at 77 K with a Micromeritics 3020 instrument. Transmission electron microscopy (TEM) images were obtained by a Hitachi HT-7700 electron microscope operated at an accelerating voltage of 100 kV. Fourier transformed infrared (FTIR) spectra were recorded on a Bruker VERTEX 700 spectrometer between 4000 and 600 cm^{-1} . Diffuse reflection spectra (DRS) were obtained on a Hitachi U-3010 UV-vis spectrophotometer. Photoluminescence spectra (PL) of the samples were obtained at room temperature excited by incident light of 318 nm using a fluorescence spectrometer (JASCO FP-6500).

Photocatalytic Tests and Photoelectrochemical Performance. Photocatalytic activities were evaluated by the degradation of methylene blue (MB) and phenol under visible light and simulated solar irradiation. Visible light irradiation was provided by a 500 W xenon lamp with a 420 nm cutoff filter, and the average visible light intensity was 40.0 $\text{mW}\cdot\text{cm}^{-2}$. Simulated solar irradiation was provided by a 500 W xenon lamp without the cutoff filter. The radiant flux was measured by a power meter from the Institute of Electric Light Source (Beijing). In each run, 50 mL of MB solution ($3.0 \times 10^{-5} \text{ M}$) or phenol solution ($5.0 \text{ mg}\cdot\text{L}^{-1}$) containing 25 mg of as-synthesized photocatalyst was placed in a glass beaker. Before irradiation, the suspensions were magnetically stirred in the dark for 2 h to ensure equilibrium between the photocatalyst and target pollutant. At certain time intervals, 2 mL of the suspensions was taken and centrifuged to remove the particles. The concentration of MB was analyzed by recording the absorption intensity at 663 nm using a Hitachi U-3010 UV-vis spectrophotometer. The intermediates of MB were analyzed using a Lumtech HPLC with a UV absorbance detector (K 2501) operated at 292 nm coupled to a Venusil XBP-C18 (Agela Technologies Inc.) column; the mobile phase was $1.0 \text{ mL}\cdot\text{min}^{-1}$ of 40% acetonitrile and 60% 0.1 M ammonium acetate and acetic acid solution (molar ratio = 4:1). The concentration and intermediates of phenol were also analyzed using a Lumtech HPLC with a UV absorbance detector operated at 270 nm coupled to a Venusil XBP-C18 column; the mobile phase was $1.0 \text{ mL}\cdot\text{min}^{-1}$ of 60% methanol and 40% deionized water.

The electrochemical and photoelectric properties were performed on a CHI 660B electrochemical system (Shanghai, China) using a standard three-electrode cell with a working electrode, a platinum wire counter electrode, and a standard calomel electrode (SCE) reference electrode. Na_2SO_4 (0.1 M) was used as the electrolyte solution. The working electrode was prepared as follows: 1 mg of as-prepared photocatalyst was suspended in 0.5 mL of water to produce slurry, which was then dip coated on a 20 mm \times 40 mm indium–tin oxide (ITO) glass electrode. The electrode was then exposed in air for 1 day to eliminate water and subsequently heated at 200 °C for 1 day. All investigated working electrodes were of similar thickness. Visible light irradiation was provided by a 500 W xenon lamp with a 420 nm cutoff filter. The average light intensity at the film electrode was 40.0 $\text{mW}\cdot\text{cm}^{-2}$. Potentials were obtained with reference to the SCE. The photoresponses as light on and off were measured at 0.0 V. Electrochemical impedance spectroscopy (EIS) was carried out at the open-circuit potential. A sinusoidal ac perturbation of 5 mV was applied to the electrode over the frequency range 0.05– 10^5 Hz.

RESULTS AND DISCUSSION

Structure and Morphology of Nanoporous g-C₃N₄.

The morphological structure of as-synthesized material was investigated by TEM measurement. Typical TEM images of the bulk g-C₃N₄ and optimal npg-C₃N₄ (80%) are shown in Figure 1. Bulk g-C₃N₄ displays large particles shape with a layer structure (Figure 1a); its edge area consists of several sheets, which exhibit a relatively dark brightness (Figure 1b). In Figure

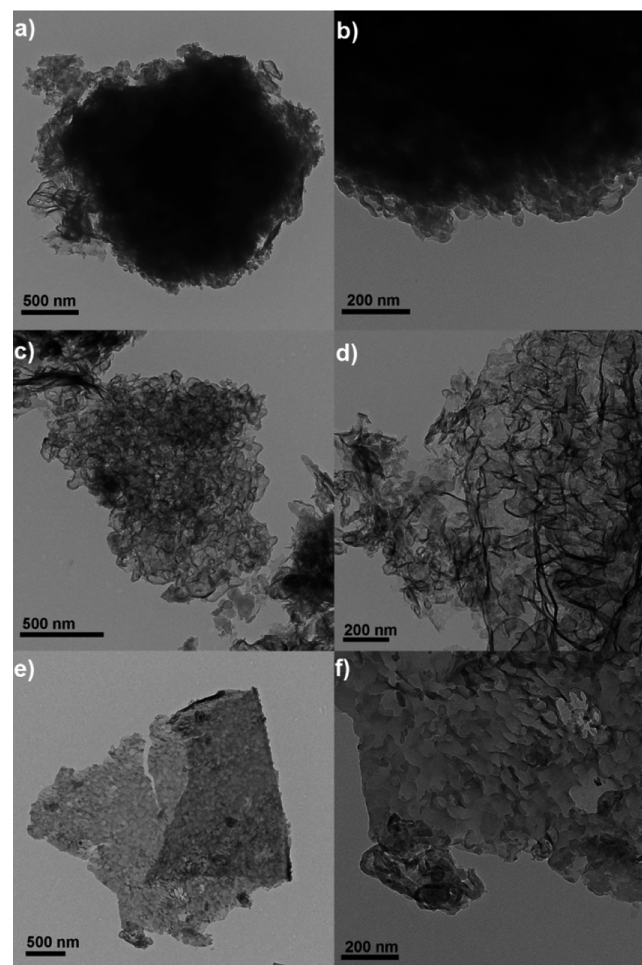


Figure 1. TEM images of the bulk g-C₃N₄ (a), sheet edge area of the bulk g-C₃N₄ (b), optimal npg-C₃N₄ (80%) (c, e), and sheet edge area of npg-C₃N₄ (80%) (d, f).

1c and 1e, npg-C₃N₄ (80%) mainly shows a flaky structure with bubble-like or irregular morphology, which looks more transparent than the bulk g-C₃N₄. These two kinds of nanoporous morphologies can be seen more clearly in its edge regions (Figure 1d and 1f). Gas bubbles produced by thiourea during calcination played an important role in the polycondensation process of dicyandiamide, which resulted in formation of nanoporosity imparted into g-C₃N₄ frameworks.²¹ Thus, thiourea is an effective bubble template. Moreover, gas bubbles produced by thiourea were uncontrollable and untunable, which resulted in formation of npg-C₃N₄ with different kinds of nanoporous morphology (Figure 1c and Figure 1e).

In order to measure the nanoporous structure in detail, the BET surface area and pore size distribution were analyzed. As can be seen in Figure 2a, the BET surface area of npg-C₃N₄ progressively increases with the rising proportion of thiourea. The surface area of npg-C₃N₄ (80%) is $46.4 \text{ m}^2\cdot\text{g}^{-1}$, which is about 3.4 times as high as that of the bulk g-C₃N₄ ($13.6 \text{ m}^2\cdot\text{g}^{-1}$). Additionally, compared with the bulk g-C₃N₄, increasingly apparent pore size distribution curves of npg-C₃N₄ can be observed with the rising proportion of thiourea (Figure 2b), which mainly distribute at about 3.7 nm, and have a broad peak at 5–70 nm.³⁵ Thus, the rising proportion of thiourea can decompose into more gas bubbles during the polycondensation

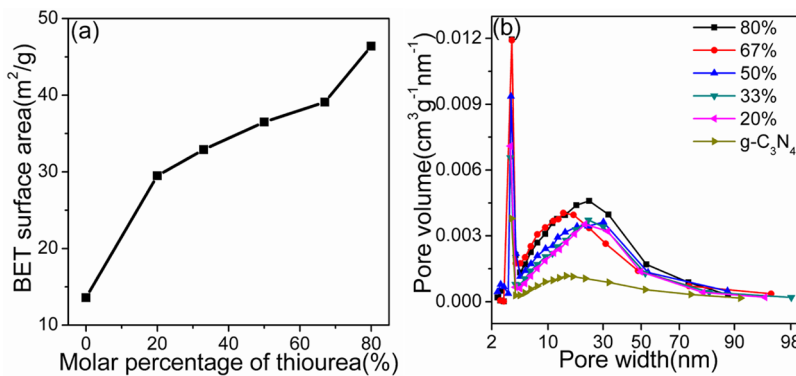


Figure 2. (a) BET surface area; (b) pore size distribution of the bulk g-C₃N₄ and npg-C₃N₄ of different thiourea molar percentages.

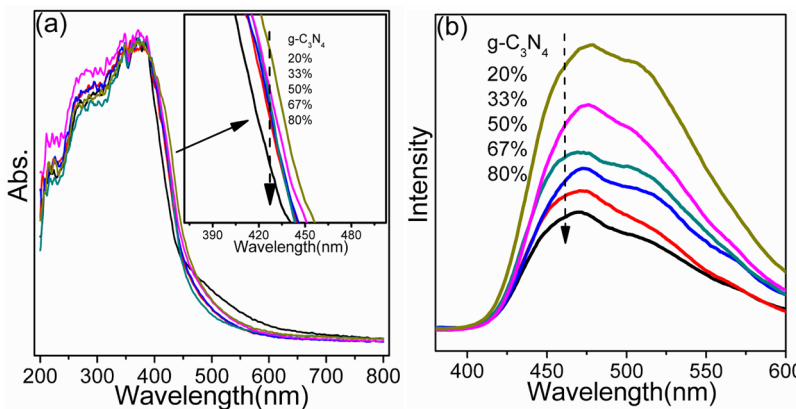


Figure 3. (a) DRS spectra; (b) PL spectra (under photoexcitation at 318 nm) of the bulk g-C₃N₄ and npg-C₃N₄ of different thiourea molar percentages.

process, leading to npg-C₃N₄ with more apparent nanoporous structure.

XRD patterns of the bulk g-C₃N₄ and npg-C₃N₄ of different thiourea molar percentages are shown in Figure S1 (Supporting Information). For the bulk g-C₃N₄, the sharp 002 diffraction peak at 27.5° indicates the characteristic interlayer stacking structure of aromatic systems, revealing an interlayer spacing of about 0.324 nm. The 100 diffraction peak at 13.1° relates to the interplanar structural packing, such as the hole-to-hole distance of the nitride pores in the crystal, corresponding to an interlayer spacing of 0.675 nm.² For npg-C₃N₄ of different thiourea molar percentages, the 100 and 002 diffraction peaks are both found to be weaker and broader than that of the bulk g-C₃N₄. With the rising proportion of thiourea, the diffraction peak intensity weakens and the half-peak width increases, which should be attributed to conversion from the original graphitic-like structure to the new nanoporous structure of g-C₃N₄.³⁵

FTIR spectroscopy was studied to investigate the crystal structure of npg-C₃N₄ further. FTIR spectra of the bulk g-C₃N₄ and npg-C₃N₄ of different thiourea molar percentages (Figure S2, Supporting Information) all show typical aromatic C—N heterocycle stretches at 1200–1700 cm⁻¹, the breathing mode of the triazine units being at 806 cm⁻¹. The broad peak at 2900–3200 cm⁻¹ is attributed to the N—H and O—H bands, associated with the residual uncondensed amino groups and the absorbed H₂O molecules, respectively.² The npg-C₃N₄ of different thiourea molar percentages present weaker amino groups/water peaks at 2900–3200 cm⁻¹ than the bulk g-C₃N₄, indicating the nanoporous structure can improve the

polycondensation process of g-C₃N₄ via the thiourea-templated synthesis.²¹

Raman spectroscopy was carried out to study the structure changes between the bulk g-C₃N₄ and npg-C₃N₄. Raman spectra of the bulk g-C₃N₄ and npg-C₃N₄ of different thiourea molar percentages (Figure S3, Supporting Information) all show typical Raman peaks of g-C₃N₄, indicating npg-C₃N₄ retain the same crystal structure of bulk g-C₃N₄. Comparing with bulk g-C₃N₄, the npg-C₃N₄ of different thiourea molar percentages present weaker peaks at 700–720 and 1232 cm⁻¹ than the bulk g-C₃N₄, which should be also attributed to conversion from the original graphitic-like structure to the new nanoporous structure of g-C₃N₄.

The chemical states and compositions of the bulk g-C₃N₄ and npg-C₃N₄ (80%) were further investigated by XPS spectroscopy. The survey XPS spectra (Figure S4a, Supporting Information) indicate the above samples are mainly composed of C and N elements. The O element can be attributed to the absorbed H₂O or CO₂ molecules on the g-C₃N₄ surface during the polymerization process. The intensity of the O1s signal of npg-C₃N₄ (80%) is smaller than that of the bulk g-C₃N₄, indicating the nanoporous structure can improve the polycondensation process of g-C₃N₄, which is consistent with the FTIR analysis result. High-resolution spectra were taken on the C1s, N1s, and S2p regions. The C1s spectra in Figure S4b, Supporting Information, show two peaks locating at about 284.6 and 288.0 eV. The 288.0 eV peak is the main contribution, which is identified as the sp²-hybridized carbon in the triazine rings (N—C=N).²⁸ The peak at 284.6 eV is typically ascribed to sp² C—C bonds according to the literature.

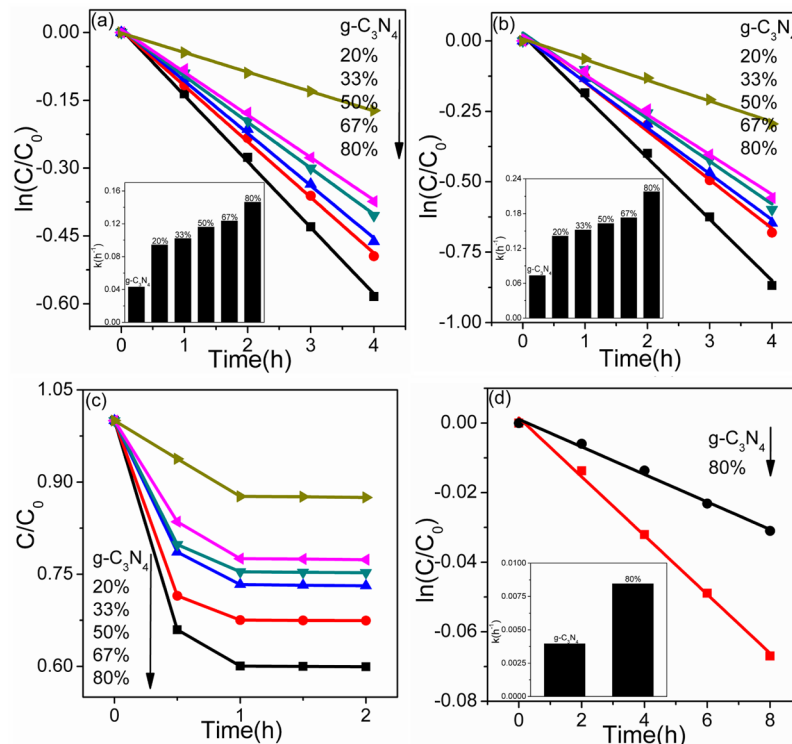


Figure 4. (a) Comparison of the photocatalytic degradation rate of MB (3.0×10^{-5} M) under visible light irradiation ($\lambda > 420$ nm) and (b) under simulated solar irradiation; (c) comparison of the adsorptivity of MB (3.0×10^{-5} M) in the dark over the bulk $\text{g-C}_3\text{N}_4$ and npg- C_3N_4 of different thiourea molar percentages; (d) comparison of the photocatalytic degradation rate of phenol (5.0 mg L^{-1}) under visible light irradiation ($\lambda > 420$ nm) over the bulk $\text{g-C}_3\text{N}_4$ and optimal npg- C_3N_4 (80%).

The main peak centered at 398.6 eV in the N1s spectra (Figure S4c, Supporting Information) corresponds to the sp^2 -bonded N involved in the triazine rings ($\text{C}-\text{N}=\text{C}$).²⁸ Compared with the bulk $\text{g-C}_3\text{N}_4$, no obvious peak shift can be found in the C1s and N1s spectra of npg- C_3N_4 (80%), suggesting that the chemical states of both carbon and nitrogen in npg- C_3N_4 (80%) are almost the same as in the bulk $\text{g-C}_3\text{N}_4$. There is no signal assigned to the sulfur species in the S2p spectra (Figure S4d, Supporting Information), which proves that the function of the sulfur species of thiourea is to modulate the $\text{g-C}_3\text{N}_4$ morphology instead of to dope the $\text{g-C}_3\text{N}_4$ semiconductor.

The optical properties of the samples were investigated by DRS and PL measurement. DRS spectra of the bulk $\text{g-C}_3\text{N}_4$ and npg- C_3N_4 of different thiourea molar percentages are shown in Figure 3a. It can be seen that the bulk $\text{g-C}_3\text{N}_4$ shows light absorbance in a wide range from UV to visible wavelength. With the increasing proportion of thiourea, the absorption edge of npg- C_3N_4 shows a gradual blue shift from 475 nm of the bulk $\text{g-C}_3\text{N}_4$ to 459 nm of npg- C_3N_4 (80%). This blue shift performance of npg- C_3N_4 can be presumably ascribed to its nanoporous structure, which can result in the quantum confinement effect.²⁸ Moreover, this blue shift indicates enlarged band gaps in npg- C_3N_4 . The enlarged band gaps of npg- C_3N_4 leads to a strengthened redox ability, which can result in enhanced photocatalytic activity.²⁸

PL spectra of the bulk $\text{g-C}_3\text{N}_4$ and npg- C_3N_4 of different thiourea molar percentages under photoexcitation at 318 nm are shown in Figure 3b. With the increasing proportion of thiourea, the position of the emission peak of npg- C_3N_4 also exhibits a gradual blue shift from 479 nm of the bulk $\text{g-C}_3\text{N}_4$ to 470 nm of npg- C_3N_4 (80%), which is in accordance with the result of DRS spectra.²⁶

Enhancement of Photocatalytic Activity and Photo-current.

The photocatalytic performance was mainly evaluated by degradation of methylene blue (MB), a hazardous dye as well as a common model to test the photodegradation activity. The photocatalytic degradation process follows the pseudo-first-order kinetics, and the value of the rate constant k is equal to the corresponding slope of the fitting line.³⁷ As shown in Figure 4a, under visible light irradiation ($\lambda > 420$ nm), the photodegradation activity of npg- C_3N_4 gradually increases with the rising proportion of thiourea. The npg- C_3N_4 (80%) has the highest apparent k of 0.146 h^{-1} , which is almost 3.4 times as high as that of the bulk $\text{g-C}_3\text{N}_4$ (0.0430 h^{-1}). Under simulated solar irradiation, npg- C_3N_4 also exhibits gradual enhanced photodegradation activity with the increasing proportion of thiourea (Figure 4b). The apparent k of npg- C_3N_4 (80%) (0.218 h^{-1}) is the best, which is almost 2.0 times better than that of the bulk $\text{g-C}_3\text{N}_4$ (0.0734 h^{-1}).

The HPLC chromatograms of the MB solution initially and after different irradiation times of photocatalytic degradation over optimal npg- C_3N_4 (80%) were recorded and are shown in Figure S5, Supporting Information. We find the gradual decrease of the MB peak intensity at 5.9 min and the appearance of new peaks emerged at lower retention times after 4 h of photodegradation, indicating formation of new intermediates. Consequently, photodegradation of the MB solutions not only caused its decoloration but also fractionally destroyed the structure of the MB molecules. According to the literature, the intermediates at 4.0 and 4.9 min are attributed to azure A (AA) and azure B (AB), which could be formed through demethylation cleavage of one or two methyl group substituents on the amine groups during photodegradation.³⁸

Adsorption experiments in the dark were achieved to evaluate the adsorptivity of the photocatalysts (Figure 4c). The adsorption achieved equilibrium within 1 h, the adsorptivity of npg-C₃N₄ increases with the rising proportion of thiourea, and 12.5% and 40.0% of MB are adsorbed from the solution by the bulk g-C₃N₄ and npg-C₃N₄ (80%), respectively. The enhancement of adsorption could be interpreted by the great difference in the surface area between the bulk g-C₃N₄ and npg-C₃N₄ (80%) (13.6 and 46.4 m²·g⁻¹, respectively).

Photodegradation of phenol over the bulk g-C₃N₄ and optimal npg-C₃N₄ (80%) (Figure 4d) was also investigated under visible light irradiation ($\lambda > 420$ nm). The apparent k of npg-C₃N₄ (80%) is 0.00846 h⁻¹, which is almost 2.1 times in comparison of that of the bulk g-C₃N₄ (0.00396 h⁻¹).

The HPLC chromatograms of the phenol solution initially and after different irradiation times of photocatalytic degradation over optimal npg-C₃N₄ (80%) were also studied. As shown in Figure S6, Supporting Information, the phenol peak intensity at 5.3 min decreased gradually and a new peak intensity at 2.1 min increased after 8 h of photodegradation, indicating formation of a new intermediate. According to the literature, the intermediate at 2.1 min is attributed to hydroquinone (HQ) formed during phenol oxidation.³⁹

Photocurrent measurements of the bulk g-C₃N₄ and optimal npg-C₃N₄ (80%) electrodes were also investigated (Figure 5).

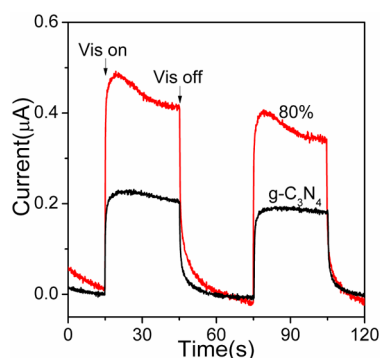


Figure 5. Photocurrent measurements under visible light irradiation ($\lambda > 420$ nm) of the bulk g-C₃N₄ and optimal npg-C₃N₄ (80%) electrodes.

A fast and uniform photocurrent response was observed for each switch-on and switch-off event in both electrodes under visible light irradiation ($\lambda > 420$ nm). The photocurrent of npg-

C₃N₄ (80%) electrode is about 2.0 times as high as that of the bulk g-C₃N₄ electrode, which indicates that the separation efficiency of photogenerated electrons and holes is significantly improved in npg-C₃N₄.⁴⁰

Effect of the Heating Rate. The effect of heating rate on the structure and photocatalytic activity of npg-C₃N₄ was also investigated under different heating rates during calcination. The npg-C₃N₄ prepared in the same thiourea molar percentage of 20% under different heating rates of 8, 6, 4, and 2 °C min⁻¹ from RT to 300 °C were named as 8, 6, 4, and 2 °C·min⁻¹, respectively.

As can be seen in Figure 6a, the BET surface area of npg-C₃N₄ progressively increases with the rising heating rate. The BET surface area of npg-C₃N₄ (8 °C·min⁻¹) is 29.5 m²·g⁻¹, which is about 1.3 times as high as that of npg-C₃N₄ (2 °C·min⁻¹) (23.1 m²·g⁻¹). Increasingly apparent pore size distribution curves of npg-C₃N₄ can be observed as the heating rate raised (Figure S7a, Supporting Information), which also mainly distribute at about 3.7 nm, and have a broad peak at 5–70 nm.³⁵ Thus, a higher heating rate may promote more complete decomposition of thiourea and produce more gas bubbles as well, which result in npg-C₃N₄ with more apparent nanoporous structure.

Figure 6b shows the comparison of the photocatalytic degradation rate constant k of MB over npg-C₃N₄ prepared under different heating rates. Under visible light irradiation ($\lambda > 420$ nm), the photodegradation activity of npg-C₃N₄ gradually increases with the increasing heating rate. The npg-C₃N₄ (8 °C·min⁻¹) has the highest apparent k of 0.0931 h⁻¹, which is almost 1.4 times as high as that of npg-C₃N₄ (2 °C·min⁻¹) (0.0679 h⁻¹). The adsorptivity of npg-C₃N₄ prepared under different heating rates was also studied (Figure S7b, Supporting Information). The adsorption achieved equilibrium within 1 h, the adsorption capacity of npg-C₃N₄ increases with the rising heating rate, and 15.7% and 23.0% of MB are adsorbed from the solution by npg-C₃N₄ (2 °C·min⁻¹) and npg-C₃N₄ (8 °C·min⁻¹), respectively.

The above results indicate that npg-C₃N₄ prepared under a higher heating rate can possess a larger surface area and more apparent nanoporous structure, which result in improved adsorption and photodegradation activities under visible light irradiation. Therefore, we previously chose to synthesize npg-C₃N₄ of different thiourea molar percentages under a heating rate of 8 °C·min⁻¹.

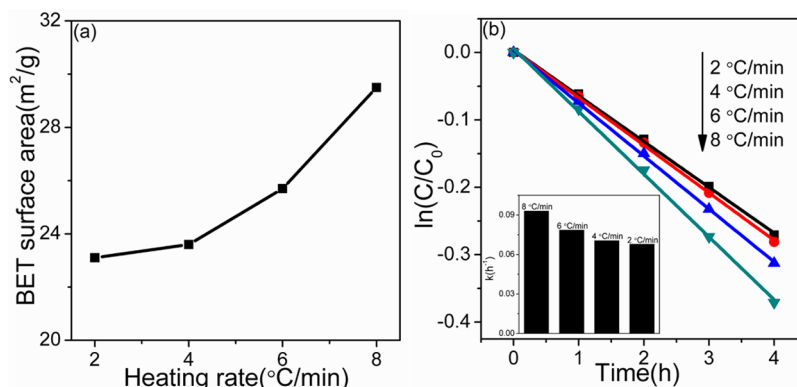


Figure 6. (a) BET surface area; (b) comparison of the photocatalytic degradation rate of MB (3.0×10^{-5} M) under visible light irradiation ($\lambda > 420$ nm) over npg-C₃N₄ prepared under different heating rates.

Mechanism of the Enhancement of Photoactivity. The greatly enhanced adsorption capacity for the target pollutants, photocatalytic degradation, and photocurrent performances of npg-C₃N₄ over the bulk g-C₃N₄ can be attributed to four main reasons: (i) the surface area of npg-C₃N₄ is much larger than that of the bulk g-C₃N₄, and the increased surface area offers more surface active sites for adsorption and photocatalytic reaction;⁶ (ii) the adsorptivity of npg-C₃N₄ is much better than that of the bulk g-C₃N₄, and the improved adsorptivity for the target pollutants could accelerate the photodegradation reaction;⁴¹ (iii) the separation of photogenerated electron–hole pairs and the charge immigration of npg-C₃N₄ are more effective, and the nanoporous structure can reduce the distance for the charge carriers to transfer from the place generated to the solid–liquid interface and suppress recombination of photogenerated electron–hole pairs during the immigration due to its thin thickness;⁴² (iv) the band gap of npg-C₃N₄ is enlarged due to the quantum confinement effect, and the enlarged band gap of npg-C₃N₄ leads to a strengthened redox ability which results in an enhanced photocatalytic activity.

The effect of nanoporous structure on the kinetics of interfacial charge immigration was further investigated by EIS analysis.⁴³ Figure 7 shows the EIS Nyquist plots of the bulk g-

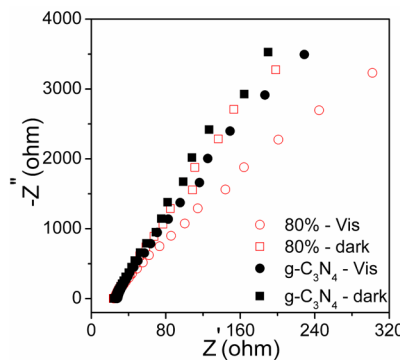


Figure 7. EIS Nyquist plots under visible light irradiation ($\lambda > 420$ nm) of the bulk g-C₃N₄ and optimal npg-C₃N₄ (80%) electrodes.

C₃N₄ and optimal npg-C₃N₄ (80%) electrodes under dark condition or visible light irradiation ($\lambda > 420$ nm). The arc radius on the EIS Nyquist plot can reflect the reaction rate on the surface of the electrode. A smaller arc radius corresponds to a more effective separation of photogenerated electron–hole pairs and a higher efficiency of charge immigration across the electrode/electrolyte interface.⁴⁴ The arc radii of npg-C₃N₄ (80%) electrode are smaller than that of the bulk g-C₃N₄ electrode, suggesting that the nanoporous structure can make the separation and immigration of photogenerated electron–hole pairs more efficient, which is in good accordance with the result of the photocurrent measurement.

CONCLUSIONS

We developed a facile bubble-templating method to synthesize npg-C₃N₄ using dicyandiamide as the precursor and thiourea as the bubble template. A higher calcination heating rate and proportion of thiourea can result in a larger surface area and better adsorption and photodegradation activities of npg-C₃N₄. Compared with the bulk g-C₃N₄, npg-C₃N₄ possesses improved separation of photogenerated electron–hole pairs and higher efficiency of charge immigration. Therefore, the adsorption capacity for the target pollutants and the photocatalytic

degradation and photocurrent performances under visible light irradiation of npg-C₃N₄ are much higher than that of the bulk g-C₃N₄. This work may give insight into a general approach for promising porous g-C₃N₄ and their application in environment purification and solar energy conversion.

ASSOCIATED CONTENT

S Supporting Information

XRD patterns, FTIR spectra, Raman spectra, and XPS spectra of the bulk g-C₃N₄ and npg-C₃N₄ of different thiourea molar percentages, HPLC chromatograms of the MB and phenol solution initially and after different irradiation times of photocatalytic degradation over optimal npg-C₃N₄ (80%), pore size distribution and comparison of the adsorptivity of MB (3.0×10^{-5} M) in the dark over npg-C₃N₄ prepared under different heating rates. This material is available free of charge via the Internet at <http://pubs.acs.org>.

AUTHOR INFORMATION

Corresponding Author

*Phone: +86-10-62787601. Fax: +86-10-62787601. E-mail: zhuyf@tsinghua.edu.cn.

Author Contributions

[†]These authors contributed equally to this work.

Notes

The authors declare no competing financial interest.

ACKNOWLEDGMENTS

This work was partly supported by National Basic Research Program of China (973 Program) (2013CB632403), National High Technology Research and Development Program of China (2012AA062701), National Natural Science Foundation of China (20925725 and 50972070), and Atmospheric Environment Monitoring & Pollution Control Program of Jiangsu Province (AEMPC201103).

REFERENCES

- (1) Maeda, K.; Wang, X. C.; Nishihara, Y.; Lu, D. L.; Antonietti, M.; Domen, K. Photocatalytic activities of graphitic carbon nitride powder for water reduction and oxidation under visible light. *J. Phys. Chem. C* **2009**, *113*, 4940–4947.
- (2) Xinchen, W.; Maeda, K.; Thomas, A.; Takanabe, K.; Gang, X.; Carlsson, J. M.; Domen, K.; Antonietti, M. A metal-free polymeric photocatalyst for hydrogen production from water under visible light. *Nat. Mater.* **2009**, *8*, 76–80.
- (3) Goettmann, F.; Fischer, A.; Antonietti, M.; Thomas, A. Metal-free catalysis of sustainable Friedel–Crafts reactions: Direct activation of benzene by carbon nitrides to avoid the use of metal chlorides and halogenated compounds. *Chem. Commun.* **2006**, 4530–4532.
- (4) Zhang, J. S.; Zhang, G. G.; Chen, X. F.; Lin, S.; Mohlmann, L.; Dolega, G.; Lipner, G.; Antonietti, M.; Blechert, S.; Wang, X. C. Co-monomer control of carbon nitride semiconductors to optimize hydrogen evolution with visible light. *Angew. Chem., Int. Ed.* **2012**, *51*, 3183–3187.
- (5) Zhang, X.; Xie, X.; Wang, H.; Zhang, J.; Pan, B.; Xie, Y. Enhanced photoresponsive ultrathin graphitic-phase C₃N₄ nanosheets for bioimaging. *J. Am. Chem. Soc.* **2013**, *135*, 18–21.
- (6) Zheng, Y.; Liu, J.; Liang, J.; Jaroniec, M.; Qiao, S. Z. Graphitic carbon nitride materials: Controllable synthesis and applications in fuel cells and photocatalysis. *Energy Environ. Sci.* **2012**, *5*, 6717–6731.
- (7) Ding, Z.; Chen, X.; Antonietti, M.; Wang, X. Synthesis of transition metal-modified carbon nitride polymers for selective hydrocarbon oxidation. *ChemSusChem* **2011**, *4*, 274–281.

- (8) Di, Y.; Wang, X. C.; Thomas, A.; Antonietti, M. Making metal-carbon nitride heterojunctions for improved photocatalytic hydrogen evolution with visible light. *ChemCatChem* **2010**, *2*, 834–838.
- (9) Zhang, J. S.; Sun, J. H.; Maeda, K.; Domen, K.; Liu, P.; Antonietti, M.; Fu, X. Z.; Wang, X. C. Sulfur-mediated synthesis of carbon nitride: Band-gap engineering and improved functions for photocatalysis. *Energy Environ. Sci.* **2011**, *4*, 675–678.
- (10) Yan, S. C.; Lv, S. B.; Li, Z. S.; Zou, Z. G. Organic-inorganic composite photocatalyst of g-C₃N₄ and TaON with improved visible light photocatalytic activities. *Dalton Trans.* **2010**, *39*, 1488–1491.
- (11) Chen, X. F.; Zhang, J. S.; Fu, X. Z.; Antonietti, M.; Wang, X. C. Fe-g-C₃N₄-catalyzed oxidation of benzene to phenol using hydrogen peroxide and visible light. *J. Am. Chem. Soc.* **2009**, *131*, 11658–11659.
- (12) Yan, S. C.; Li, Z. S.; Zou, Z. G. Photodegradation of rhodamine B and methyl orange over boron-doped g-C₃N₄ under visible light irradiation. *Langmuir* **2010**, *26*, 3894–3901.
- (13) Liao, G. Z.; Chen, S.; Quan, X.; Yu, H. T.; Zhao, H. M. Graphene oxide modified g-C₃N₄ hybrid with enhanced photocatalytic capability under visible light irradiation. *J. Mater. Chem.* **2012**, *22*, 2721–2726.
- (14) Yue, B.; Li, Q. Y.; Iwai, H.; Kako, T.; Ye, J. H. Hydrogen production using zinc-doped carbon nitride catalyst irradiated with visible light. *Sci. Technol. Adv. Mater.* **2011**, *12*, 034401.
- (15) Meng, Y. L.; Shen, J.; Chen, D.; Xin, G. Photodegradation performance of methylene blue aqueous solution on Ag/g-C₃N₄ catalyst. *Rare Met.* **2011**, *30*, 276–279.
- (16) Zhang, Y.; Mori, T.; Ye, J.; Antonietti, M. Phosphorus-doped carbon nitride solid: Enhanced electrical conductivity and photo-current generation. *J. Am. Chem. Soc.* **2010**, *132*, 6294–6295.
- (17) Liu, G.; Niu, P.; Sun, C. H.; Smith, S. C.; Chen, Z. G.; Lu, G. Q.; Cheng, H. M. Unique electronic structure induced high photo-reactivity of sulfur-doped graphitic C₃N₄. *J. Am. Chem. Soc.* **2010**, *132*, 11642–11648.
- (18) Niu, P.; Zhang, L.; Liu, G.; Cheng, H. M. Graphene-like carbon nitride nanosheets for improved photocatalytic activities. *Adv. Funct. Mater.* **2012**, *22*, 4763–4770.
- (19) Su, F. Z.; Mathew, S. C.; Mohlmann, L.; Antonietti, M.; Wang, X. C.; Blechert, S. Aerobic oxidative coupling of amines by carbon nitride photocatalysis with visible light. *Angew. Chem., Int. Ed.* **2011**, *50*, 657–660.
- (20) Lin, Z.; Wang, X. Nanostructure engineering and doping of conjugated carbon nitride semiconductors for hydrogen photosynthesis. *Angew. Chem., Int. Ed.* **2013**, *52*, 1735–1738.
- (21) Guigang, Z.; Jinshui, Z.; Mingwen, Z.; Xinchen, W. Polycondensation of thiourea into carbon nitride semiconductors as visible light photocatalysts. *J. Mater. Chem.* **2012**, *22*, 8083–8091.
- (22) Jin, X.; Balasubramanian, V. V.; Selvan, S. T.; Sawant, D. P.; Chari, M. A.; Lu, G. Q.; Vinu, A. Highly ordered mesoporous carbon nitride nanoparticles with high nitrogen content: A metal-free basic catalyst. *Angew. Chem., Int. Ed.* **2009**, *48*, 7884–7887.
- (23) Lee, E. Z.; Jun, Y. S.; Hong, W. H.; Thomas, A.; Jin, M. M. Cubic mesoporous graphitic carbon(IV) nitride: An all-in-one chemosensor for selective optical sensing of metal ions. *Angew. Chem., Int. Ed.* **2010**, *49*, 9706–9710.
- (24) Liang, J.; Zheng, Y.; Chen, J.; Liu, J.; Hulicova-Jurcakova, D.; Jaroniec, M.; Qiao, S. Z. Facile oxygen reduction on a three-dimensionally ordered macroporous graphitic C₃N₄/carbon composite electrocatalyst. *Angew. Chem., Int. Ed.* **2012**, *51*, 3892–3896.
- (25) Goettmann, F.; Fischer, A.; Antonietti, M.; Thomas, A. Chemical synthesis of mesoporous carbon nitrides using hard templates and their use as a metal-free catalyst for Friedel-Crafts reaction of benzene. *Angew. Chem., Int. Ed.* **2006**, *45*, 4467–4471.
- (26) Chen, X. F.; Jun, Y. S.; Takanabe, K.; Maeda, K.; Domen, K.; Fu, X. Z.; Antonietti, M.; Wang, X. C. Ordered mesoporous SBA-15 type graphitic carbon nitride: A semiconductor host structure for photocatalytic hydrogen evolution with visible light. *Chem. Mater.* **2009**, *21*, 4093–4095.
- (27) Vinu, A.; Ariga, K.; Mori, T.; Nakanishi, T.; Hishita, S.; Golberg, D.; Bando, Y. Preparation and characterization of well-ordered hexagonal mesoporous carbon nitride. *Adv. Mater.* **2005**, *17*, 1648–1652.
- (28) Cui, Y. J.; Zhang, J. S.; Zhang, G. G.; Huang, J. H.; Liu, P.; Antonietti, M.; Wang, X. C. Synthesis of bulk and nanoporous carbon nitride polymers from ammonium thiocyanate for photocatalytic hydrogen evolution. *J. Mater. Chem.* **2011**, *21*, 13032–13039.
- (29) Groenewolt, M.; Antonietti, M. Synthesis of g-C₃N₄ nanoparticles in mesoporous silica host matrices. *Adv. Mater.* **2005**, *17*, 1789–1792.
- (30) Hwang, S.; Lee, S.; Yu, J. S. Template-directed synthesis of highly ordered nanoporous graphitic carbon nitride through polymerization of cyanamide. *Appl. Surf. Sci.* **2007**, *253*, 5656–5659.
- (31) Vinu, A.; Srinivasu, P.; Sawant, D. P.; Mori, T.; Ariga, K.; Chang, J. S.; Jhung, S. H.; Balasubramanian, V. V.; Hwang, Y. K. Three-dimensional cage type mesoporous CN-Based hybrid material with very high surface area and pore volume. *Chem. Mater.* **2007**, *19*, 4367–4372.
- (32) Vinu, A. Two-dimensional hexagonally-ordered mesoporous carbon nitrides with tunable pore diameter, surface area and nitrogen content. *Adv. Funct. Mater.* **2008**, *18*, 816–827.
- (33) Thomas, A.; Fischer, A.; Goettmann, F.; Antonietti, M.; Muller, J. O.; Schlogl, R.; Carlsson, J. M. Graphitic carbon nitride materials: Variation of structure and morphology and their use as metal-free catalysts. *J. Mater. Chem.* **2008**, *18*, 4893–4908.
- (34) Takanabe, K.; Kamata, K.; Wang, X.; Antonietti, M.; Kubota, J.; Domen, K. Photocatalytic hydrogen evolution on dye-sensitized mesoporous carbon nitride photocatalyst with magnesium phthalocyanine. *Phys. Chem. Chem. Phys.* **2010**, *12*, 13020–13025.
- (35) Wang, X. C.; Maeda, K.; Chen, X. F.; Takanabe, K.; Domen, K.; Hou, Y. D.; Fu, X. Z.; Antonietti, M. Polymer semiconductors for artificial photosynthesis: Hydrogen evolution by mesoporous graphitic carbon nitride with visible light. *J. Am. Chem. Soc.* **2009**, *131*, 1680–1681.
- (36) Wang, Y.; Zhang, J. S.; Wang, X. C.; Antonietti, M.; Li, H. R. Boron- and fluorine-containing mesoporous carbon nitride polymers: Metal-free catalysts for cyclohexane oxidation. *Angew. Chem., Int. Ed.* **2010**, *49*, 3356–3359.
- (37) Terzian, R.; Serpone, N.; Minero, C.; Pelizzetti, E. Photocatalyzed mineralization of cresols in aqueous media with irradiated Titania. *J. Catal.* **1991**, *128*, 352–365.
- (38) Rauf, M. A.; Meetani, M. A.; Khaleel, A.; Ahmed, A. Photocatalytic degradation of methylene blue using a mixed catalyst and product analysis by LC/MS. *Chem. Eng. J.* **2010**, *157*, 373–378.
- (39) Azevedo, E. B.; Neto, F. R. D.; Dezotti, M. TiO₂-photocatalyzed degradation of phenol in saline media: Lumped kinetics, intermediates, and acute toxicity. *Appl. Catal. B: Environ.* **2004**, *54*, 165–173.
- (40) Zhang, Y. J.; Thomas, A.; Antonietti, M.; Wang, X. C. Activation of carbon nitride solids by protonation: Morphology changes, enhanced ionic conductivity, and photoconduction experiments. *J. Am. Chem. Soc.* **2009**, *131*, 50–51.
- (41) Zhang, H.; Lv, X. J.; Li, Y. M.; Wang, Y.; Li, J. H. P25-graphene composite as a high performance photocatalyst. *ACS Nano* **2010**, *4*, 380–386.
- (42) Carraway, E. R.; Hoffman, A. J.; Hoffmann, M. R. Photocatalytic oxidation of organic acids on quantum-sized semiconductor colloids. *Environ. Sci. Technol.* **1994**, *28*, 786–793.
- (43) Li, J.; Zheng, L.; Li, L.; Xian, Y.; Jin, L. Fabrication of TiO₂/Ti electrode by laser-assisted anodic oxidation and its application on photoelectrocatalytic degradation of methylene blue. *J. Hazard. Mater.* **2007**, *139*, 72–78.
- (44) Hong, S. J.; Lee, S.; Jang, J. S.; Lee, J. S. Heterojunction BiVO₄/WO₃ electrodes for enhanced photoactivity of water oxidation. *Energy Environ. Sci.* **2011**, *4*, 1781–1787.